

# Designing Boron Nitride Islands in Carbon Materials for Efficient Electrochemical Synthesis of Hydrogen Peroxide

Shucheng Chen,<sup>†,‡,ID</sup> Zhihua Chen,<sup>†,§</sup> Samira Siahrostami,<sup>†,||</sup> Drew Higgins,<sup>†,ID</sup> Dennis Nordlund,<sup>‡</sup> Dimosthenis Sokaras,<sup>‡</sup> Taeho Roy Kim,<sup>§</sup> Yunzhi Liu,<sup>§</sup> Xuzhou Yan,<sup>†,ID</sup> Elisabeth Nilsson,<sup>||</sup> Robert Sinclair,<sup>§</sup> Jens K. Nørskov,<sup>\*,†,||</sup> Thomas F. Jaramillo,<sup>\*,†,||,ID</sup> and Zhenan Bao<sup>\*,†,ID</sup>

<sup>†</sup>SUNCAT Center for Interface Science and Catalysis, Department of Chemical Engineering, Stanford University, Stanford, California 94305, United States

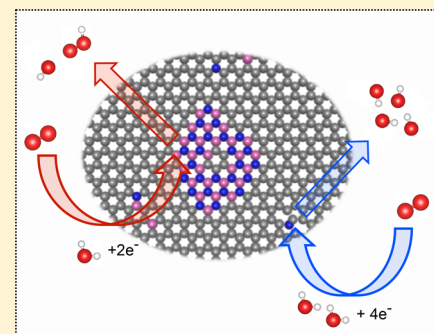
<sup>‡</sup>Stanford Synchrotron Radiation Light Source, SLAC National Accelerator Laboratory, Menlo Park, California 94025, United States

<sup>§</sup>Department of Materials Science and Engineering, Stanford University, Stanford, California 94305, United States

<sup>||</sup>SUNCAT Center for Interface Science and Catalysis, SLAC National Accelerator Laboratory, Menlo Park, California 94025, United States

## Supporting Information

**ABSTRACT:** Heteroatom-doped carbons have drawn increasing research interest as catalysts for various electrochemical reactions due to their unique electronic and surface structures. In particular, co-doping of carbon with boron and nitrogen has been shown to provide significant catalytic activity for oxygen reduction reaction (ORR). However, limited experimental work has been done to systematically study these materials, and much remains to be understood about the nature of the active site(s), particularly with regards to the factors underlying the activity enhancements of these boron–carbon–nitrogen (BCN) materials. Herein, we prepare several BCN materials experimentally with a facile and controlled synthesis method, and systematically study their electrochemical performance. We demonstrate the existence of *h*-BN domains embedded in the graphitic structures of these materials using X-ray spectroscopy. These synthesized structures yield higher activity and selectivity toward the  $2e^-$  ORR to  $H_2O_2$  than structures with individual B or N doping. We further employ density functional theory calculations to understand the role of a variety of *h*-BN domains within the carbon lattice for the ORR and find that the interface between *h*-BN domains and graphene exhibits unique catalytic behavior that can preferentially drive the production of  $H_2O_2$ . To the best of our knowledge, this is the first example of *h*-BN domains in carbon identified as a novel system for the electrochemical production of  $H_2O_2$ .



## INTRODUCTION

Heteroatom co-doping has emerged as an appealing strategy to modify the electronic and surface structures of carbon-based materials in order to tune catalytic activity toward different reactions.<sup>1–8</sup> Co-doping with boron and nitrogen is particularly attractive due to the environmental abundance of these elements, along with the ability to form a wide range of possible active sites. In extreme cases where high boron and nitrogen concentrations are used, domains of hexagonal boron nitride (*h*-BN) are formed within the carbon lattice.<sup>5,9–11</sup> Previous studies have shown that segregation of either graphene islands in a planar *h*-BN matrix, or *h*-BN islands in a graphene matrix is thermodynamically favorable.<sup>5,9–11</sup> Depending on the boron, nitrogen, and carbon stoichiometry, some hybridized and randomly distributed domains of *h*-BN and C phases can be formed with compositions ranging from pure *h*-BN to pure graphene. Such hybrid boron–carbon–nitrogen (BCN) systems provide unique electronic structures that can be used to tune the catalytic properties by varying the relative amounts of *h*-BN and graphene. Leveraging this

behavior, BCN materials have been tested as supercapacitor electrodes<sup>12,13</sup> and for several catalytic applications, such as the hydrogen evolution reaction,<sup>14</sup> oxygen evolution reaction,<sup>15</sup> and  $CO_2$  reduction reaction.<sup>16</sup>

In particular, BCN materials have recently drawn increasing interest as catalysts for the  $4e^-$  oxygen reduction reaction (ORR).<sup>17–23</sup> In many of these instances, however, the exact nature of the active-site motif in the BCN material remains elusive, and much remains to be understood toward identifying structure–activity relationships. In addition to the  $4e^-$  ORR process, the  $2e^-$  process to hydrogen peroxide ( $H_2O_2$ ) is also of particular interest for decentralized applications such as water treatment in remote areas.<sup>24</sup> Recently, theory and experiment have been used to investigate various catalysts for the electrochemical synthesis of  $H_2O_2$ , including noble metals,<sup>25–27</sup> metal alloys,<sup>26,28,29</sup> and carbon-based materials.<sup>30–35</sup> Though defective carbons have shown good activity

Received: March 13, 2018

Published: June 6, 2018



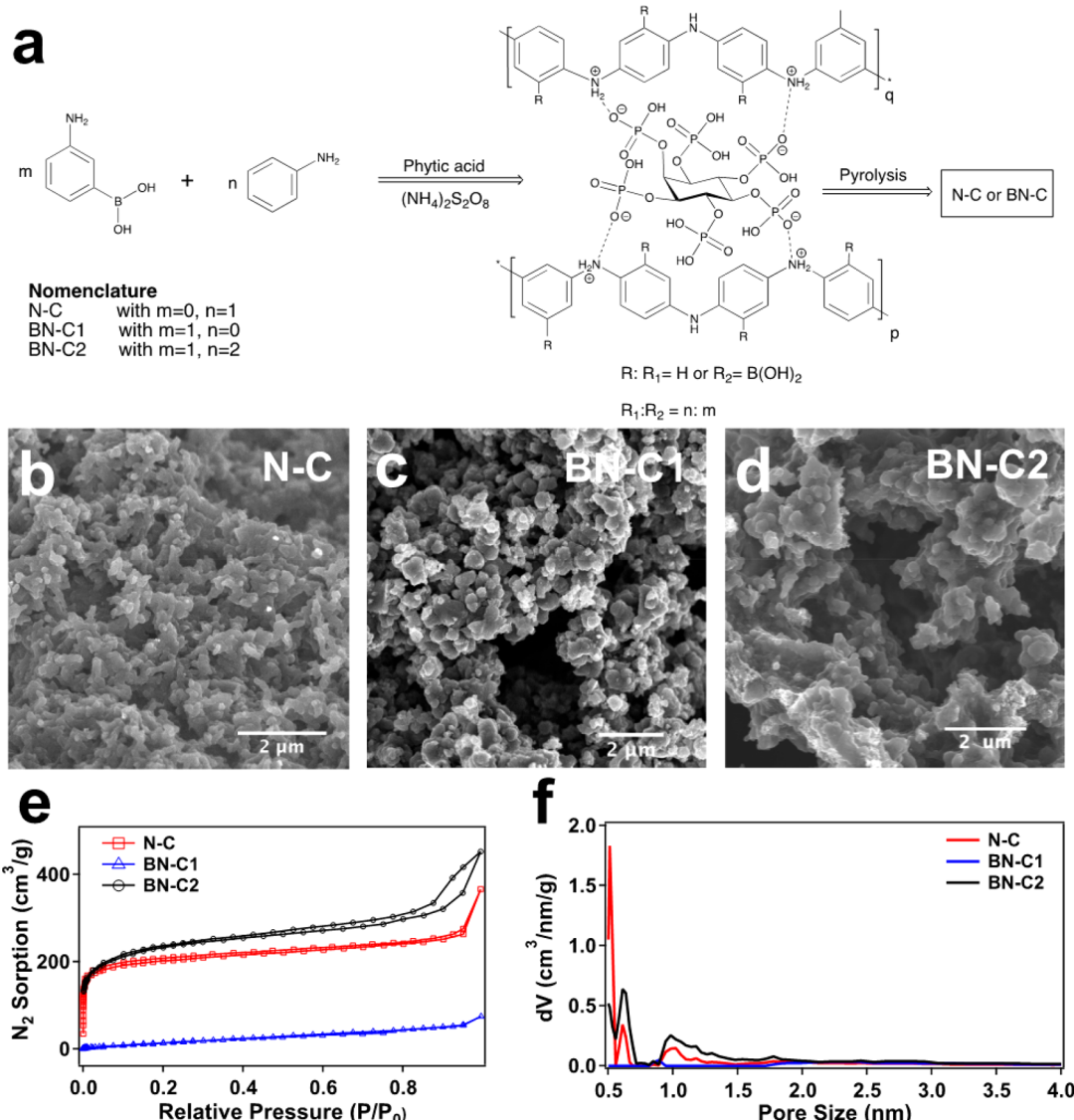


**Figure 1.** (a) Synthetic scheme for different heteroatom doped carbons. SEM images of (b) N-C, (c) BN-C1, and (d) BN-C2. (e) Nitrogen adsorption and desorption isotherms at 77 K and (f) pore size distributions of N-C, BN-C1, and BN-C2.

and selectivity toward  $\text{H}_2\text{O}_2$ , there are numerous defect-site structures that can be formed during preparation, and it is a challenge to selectively tailor synthetic processes to induce the formation of the most active and selective active-site structure(s).<sup>31,35</sup> In contrast, BCN materials provide a more tunable system since the concentration and types of B and N doping can be controlled by careful selection of synthetic conditions and precursor molecules. Furthermore, the suitability of heteroatom-doped carbon structures for  $\text{H}_2\text{O}_2$  production<sup>30,33</sup> suggests it is of interest to study the effects of B and N co-doping in an attempt to discover highly active and selective catalyst materials for this reaction.

Herein, we synthesize new B,N co-doped carbon materials and study their ORR activity and selectivity toward either the  $4\text{e}^-$  or  $2\text{e}^-$  pathway, whereby increasing selectivity toward the  $2\text{e}^-$  reduction to valuable  $\text{H}_2\text{O}_2$  products is of primary focus. We develop a facile and controllable approach, involving oxidative polymerization of a monomer containing both B and N atoms, followed by high-temperature pyrolysis to synthesize B,N co-doped porous carbon materials that allow for systematic investigation of the effects of different doping

functional groups on ORR performance. Spectroscopic characterization shows that the *h*-BN domains and N-doped sites co-exist in these graphitic structures and contribute to the observed ORR performance. We found that *h*-BN domains in graphitic structures provide higher activity and selectivity for the  $2\text{e}^-$  ORR process in comparison to individual B- or N-doped structures. To better understand how *h*-BN domains contribute to the high  $2\text{e}^-$  ORR activities, we further use density functional theory (DFT) calculations to systematically study the ORR activity of a variety of different *h*-BN compositions in a carbon lattice. We pay particular attention to a variety of possible *h*-BN/graphene interfaces and show that this interface presents intrinsically different catalytic behavior that drives the  $2\text{e}^-$  ORR, leading to  $\text{H}_2\text{O}_2$  as the major product. This is consistent with our experimental findings. This work provides insight into the development of heteroatom-doped carbon structures for electrochemical production of  $\text{H}_2\text{O}_2$ , which can be used for the design of improved catalyst materials or extended toward other reactions of interest.

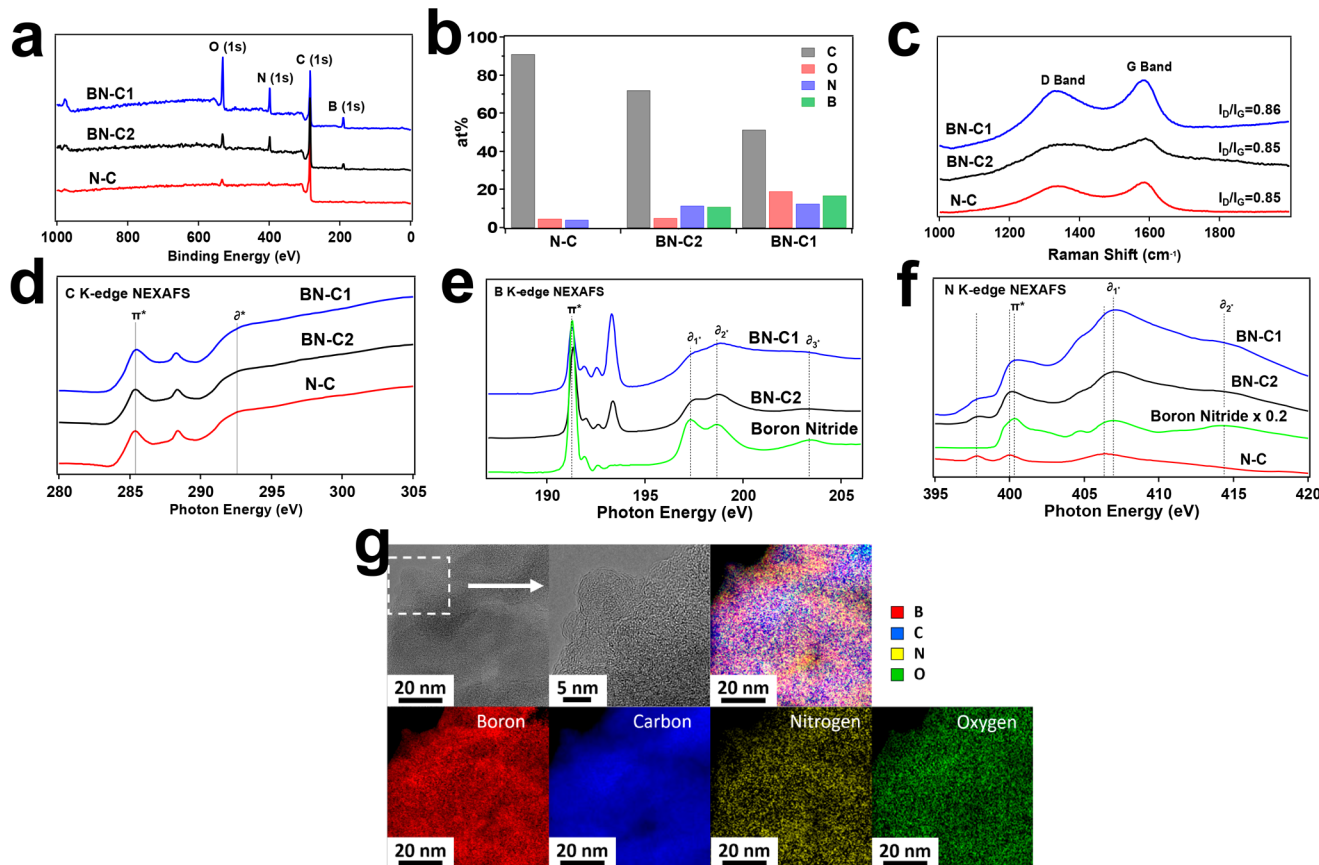


**Figure 2.** (a) XPS survey scan for N-C, BN-C1, and BN-C2. (b) Atomic composition of the four samples. (c) Raman spectra of N-C, BN-C1, and BN-C2, with  $I_D/I_G$  ratios for each sample indicated. NEXAFS spectra of (d) C-K edge, (e) B-K edge, and (f) N-K edge for N-C BN-C1, BN-C2, and *h*-BN. The intensity of N K-edge NEXAFS for boron nitride is scaled down by 5 times for easy visualization. (g) HRTEM image of an edge region of BN-C1 showing lattice fringes of the graphitic structure, along with elemental maps taken with energy filtered TEM.

## RESULTS AND DISCUSSION

**Materials Synthesis and Characterizations.** To gain a deep understanding on the effects of N doping and B<sub>x</sub>N codoping on ORR performance, we first prepared a series of carbon-based materials by varying the ratios of two different precursors during polymerization, namely aniline and 3-aminophenylboronic acid (3-APBA). This is a modified version of previously reported methods for preparing N-doped carbons from a polyaniline hydrogel precursor<sup>36,37</sup> (Figure 1a). We hypothesize it may be easier to form stable *h*-BN domains using a precursor such as 3-APBA, since both boron and nitrogen are present in the same molecule. The initial loading of boron versus nitrogen can also be tuned by changing the relative ratio of 3-APBA to aniline. Ammonium persulfate was used as the oxidant to promote the copolymerization of aniline and 3-APBA to form poly-(aniline-*co*-3-aminophenylboronic acid). Phytic acid was used as the cross-linker and also as an activation agent to create porosity and edge-site exposures in the carbon materials as shown in our previous work.<sup>36</sup> After the formation of the hydrogel, the sample was freeze-dried and then carbonized at 1000 °C for 6 h under an inert atmosphere. The final products were named as follows (refer to Figure 1a for nomenclature): N-C for samples made from only the aniline monomer ( $m = 0$ ,  $n = 1$ ); BN-C1 for samples made from only the 3-APBA monomer ( $m = 1$ ,  $n = 0$ ); and BN-C2 for both monomers with  $m = 1$ ,  $n = 2$ .

The as-synthesized samples were characterized by several different techniques. Figure 1 shows the results from SEM imaging and gas sorption measurements. For N-C made from the aniline monomer, a macroscopic network of particles was formed with micrometer-scale sized macropores (Figure 1b). The only monomer used for BN-C1 was 3-APBA, which tends to have a self-hardening effect since the polymer can be self-cross-linked through the intermolecular reaction between boronic acid groups and imines.<sup>38</sup> This leads to the formation of irregular spherical particles, as evidenced from the SEM images (Figure 1d). When the sample was made from the mixture of aniline and 3-APBA, a porous network was formed as in the case of N-C, as shown in the SEM image of BN-C2 in Figure 1c. Gas sorption testing results further confirm the effect from such co-polymerization (Figure 1e,f). BN-C1 gives a Brunauer–Emmett–Teller (BET) surface area of 74 m<sup>2</sup>/g. When two-thirds of the monomer was changed to aniline (BN-C2), the BET surface area increases significantly to 750 m<sup>2</sup>/g. Gas sorption measurements on N-C gives a comparable surface area of 630 m<sup>2</sup>/g (Figure 1e,f). All these carbon materials showed a significant fraction of micropores smaller than 2 nm.

X-ray photoelectron spectroscopy (XPS) shows that copolymerization also affects the final composition of heteroatoms (Figure 2a,b). For BN-C1, around 12.5 at% N and 16.5 at% B were doped into the sample. It is worth noting that, by incorporating B and N together, the final loading of N increased significantly from solely N-doped carbon (4 at%). This is consistent with literature findings that B and N atoms

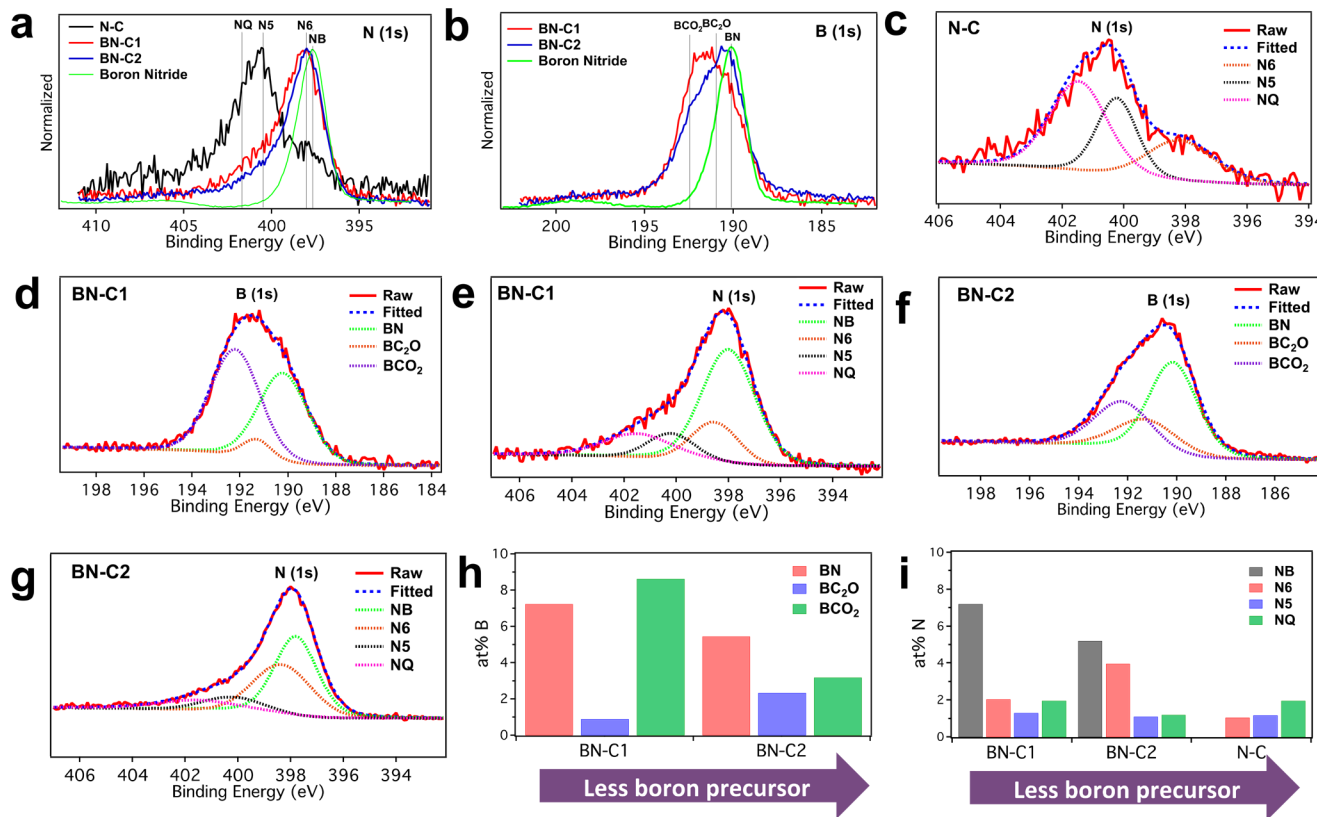


**Figure 3.** (a,b) High-resolution XPS of N 1s and B 1s for different samples. The peak positions for different types of doping motifs are indicated. (c–g) XPS fitting for N 1s and B 1s for BN-C1, BN-C2, and N-C samples. (h,i) Summary for the concentrations of different dopant types.

have strong binding and tend to form isolated patches of *h*-BN, which is the most thermodynamically stable structure in B,N co-doped graphene.<sup>8</sup> Catalyst characterization (discussed below) was consistent with the notion that *h*-BN structures were formed in these materials. For BN-C2, where less boron is introduced in the monomer precursors, the final compositions of N and B were slightly lower than for BN-C1, with about 10 at% for each element. The bulk composition of B and N in the materials was also obtained by inductively coupled plasma mass spectrometer (ICP-MS) and elemental analysis (EA). Consistent with XPS results, considerably higher concentrations of B and N were observed for BN-C1 and BN-C2 in comparison to N-C (Table S1). BN-C1 has almost 4 times more N than N-C, and also contains higher concentrations of B and N in comparison to BN-C2. It should also be noted that phytic acid and ammonia persulfate have been added as the cross-linker and oxidizer, respectively, and may introduce phosphorus and sulfur doping into the carbon structure. However, XPS showed undetectable amounts of P and S after high-temperature carbonization (Figure 2a). Raman spectroscopy showed all the samples had relatively high and similar amount of defects with  $I_D/I_G = 0.85$  (Figure 2c).

To gain more insight into the local electronic structures of these materials, and in particular to more accurately characterize the types of nitrogen and boron in the carbon structures, we employed near-edge X-ray absorption fine structure spectroscopy (NEXAFS). The C 1s NEXAFS (Figure 2d) for all samples shows the spectral fingerprints of  $\text{sp}^2$ -hybridized carbon sheets, and this is essentially unperturbed by B,N co-doping. These fingerprints consist of peaks at 285.4 and 292 eV, corresponding to the  $1s \rightarrow \pi^*$  and  $1s \rightarrow \sigma^*$  C=C bond

resonances of graphitic carbon, respectively.<sup>39,40</sup> Comparison of the B and N K-edge NEXAFS for BN-C1, BN-C2, and N-C materials with that of pure *h*-BN gives more insight on the types of the dopant bond motifs (Figure 2e,f). The close resemblance between the B and N K-edge of *h*-BN, BN-C1, and BN-C2 suggests the existence of a high concentration of  $\text{sp}^2$ -hybridized B–N bonds in BN-C and BN-C2. Both BN-C1 and BN-C2 show the characteristics of *h*-BN, with a sharp B 1s $\rightarrow\pi^*$  at about 191.3 eV and three 1s $\rightarrow\sigma^*$  resonances at 197.3, 198.7, and 203.4 eV. It is also worth noting that there is another sharp peak at 193.4 eV for BN-C1 and BN-C2 that is absent in *h*-BN. This additional peak arises from B–O motifs<sup>41</sup> and is consistent with the high amount of O content observed by XPS for these two samples (Figure 2b). N K-edge NEXAFS further confirms the clustering of B and N dopants in the BN-C1 and BN-C2 samples. Both samples show the main N 1s spectral fingerprints of *h*-BN, with a  $\pi^*$  resonance at 400.3 eV and two  $\sigma^*$  features at 407 and 414.5 eV (Figure 2f). For the N-C sample containing only N, C, and O, two main  $\pi^*$  peaks arise at 398 and 400 eV. The sharp  $\pi^*$  at 400 eV and  $\sigma^*$  at 406 eV are in close agreement with the spectrum for graphitic N, whereby a C atom in the graphitic ring structure is replaced with a N atom. On the other hand, the peak at 398 eV indicates the presence of less electronegative N-C bonds and can be assigned to pyridinic or pyrrolic N.<sup>42,43</sup> Thus, the N dopants in the N-C sample exist in the forms of mixtures of quaternary nitrogen, pyridinic nitrogen, and pyrrolic nitrogen. These two peaks are also found in the B,N co-doped samples, indicating that BN-C1 and BN-C2 consist of not only *h*-BN and boron oxide moieties but also a significant amount of single N dopant sites. While XPS and NEXAFS indicate the

**Table 1.** Summary of the Doping Type and Surface Area for Different Carbons<sup>a</sup>

sample	C (at%)	O (at%)	N (at%)	B (at%)	B and N together in h-BN domain (at%)	single N site (at%)	B in the form of BC <sub>2</sub> O (at%)	B in the form of BCO <sub>2</sub> (at%)	BET surface area (m <sup>2</sup> /g)
N-C	91.1	4.7	4.2			4.2			632
BN-C1	51.5	19.2	12.5	16.8	14.5	5.29	0.91	8.64	74
BN-C2	72.2	5.2	11.5	11	10.5	6.23	2.35	3.19	751

<sup>a</sup>All values shown are the atomic % taking into account all atoms in the sample.

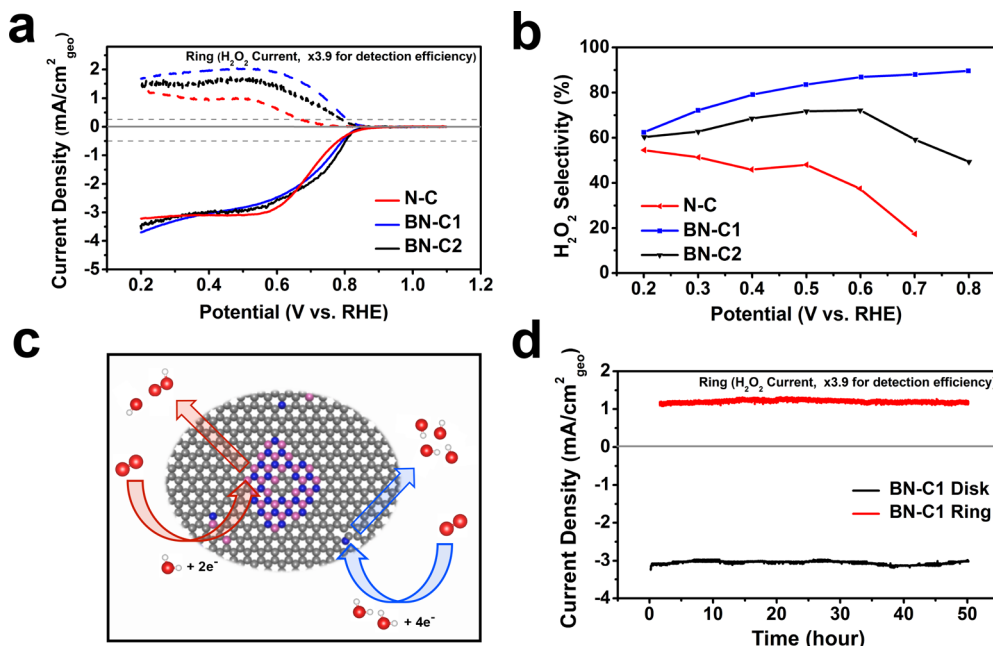


**Figure 4.** (a) RRDE voltammograms of N-C, BN-C1, and BN-C2 at 1600 rpm in O<sub>2</sub>-saturated 0.1 M KOH electrolyte with the disc current density, ring current density adjusted by collection efficiency (Pt ring, disk area 0.196 cm<sup>2</sup>, current density is normalized with respect to disk geometric area). (b) H<sub>2</sub>O<sub>2</sub> selectivity as a function of the applied potential. (c) Schematic illustration of the types of doping motifs and ORR reaction mechanisms on these active sites in the B,N co-doped samples in base condition with H<sub>2</sub>O as the proton source. Color code: C, gray; N, blue; B, red; O, white. (d) Stability performance of BN-C1 under constant potential (0.5 V vs RHE for disk and 1.2 V vs RHE for ring).

formation of *h*-BN structures in the catalyst materials, high-resolution transmission electron microscopy (HRTEM) imaging of BN-C1 (Figure 2g) was conducted to investigate the distribution of *h*-BN throughout the materials. From the energy filtered TEM images, homogeneous distribution of all four elements (B, C, N, and O) is observed. Furthermore, no phase separation between *h*-BN and graphitic carbon, nor the formation of large *h*-BN domains, was identified.

High-resolution XPS spectroscopy further supports that multiple types of B,N dopants exist in the materials. The N 1s peaks were deconvoluted, and the centers are found to be at ca. 397.9, 398.4, 400.4, and 401.5 eV, which are assigned to N–B bonding in small *h*-BN clusters, pyridinic (N6), pyrrolic (N5), and quaternary N atoms (NQ), respectively (Figure 3). Similarly, analysis of the B 1s spectra shows three peaks centered at ca. 190.0, 191.0, and 192.4 eV after deconvolution, assigned to B-N species present in small *h*-BN domains within the carbon framework, BC<sub>2</sub>O, and BCO<sub>2</sub>, respectively.<sup>21</sup> Detailed peak fitting was performed to determine the composition for each type of dopants (Figure 3c–g). As summarized in Figure 3h,i and also in Table 1, for BN-C1, approximately 7.3 at% B is in the form of *h*-BN, 0.9 at% B is in the form of BC<sub>2</sub>O, and 8.6 at% B is in the form of BCO<sub>2</sub> (total B dopant concentration is 16.8 at%). For BN-C2, where the

initial loading of B precursor is diluted with the addition of aniline, the total B atom concentration in the system decreases to 11 at%, with half of that comprised of B in the *h*-BN motifs (5.5 at% of the total atoms). For N, BN-C1, BN-C2, and N-C all exhibit single N sites (<6.5 at%) that consist of N5, N6, and NQ at different concentrations. Consistently, BN-C1 and BN-C2 show 7.2 at% N and 5.2 at% N in the form of *h*-BN, respectively. This nearly matches the results of B in the BN motif as expected, since for isolated *h*-BN clusters, the perfect ratio for B and N should be 1:1. Summarizing NEXAFS and XPS results (Table 1), it is found that BN-C1 consists of ca. 14.5 at% isolated *h*-BN clusters (consisting of ca. 7.3 at% B and 7.2 at% N of the total atoms), 4.7 at% single N sites, 19.2 at% O in the form of BC<sub>2</sub>O and BCO<sub>2</sub>, with the remaining 51.5 at % comprising C atoms. BN-C2 consists of about 10.5 at% isolated *h*-BN clusters (consisting of about 5.3 at% B and 5.2 at % N of the total atoms), ~6 at% single N sites, 5 at% O in the form of BC<sub>2</sub>O and BCO<sub>2</sub>, with the remaining 72.2 at% comprising C atoms. It is also worth noting that although BN-C1 has a high content of both O and *h*-BN, DC-4 probe measurement shows it has high electronic conductivity of 0.54 S/cm, making it well suited for electrocatalytic applications.

**ORR Performance.** The ORR activities for N-C, BN-C1, and BN-C2 were tested with a rotating ring disk electrode

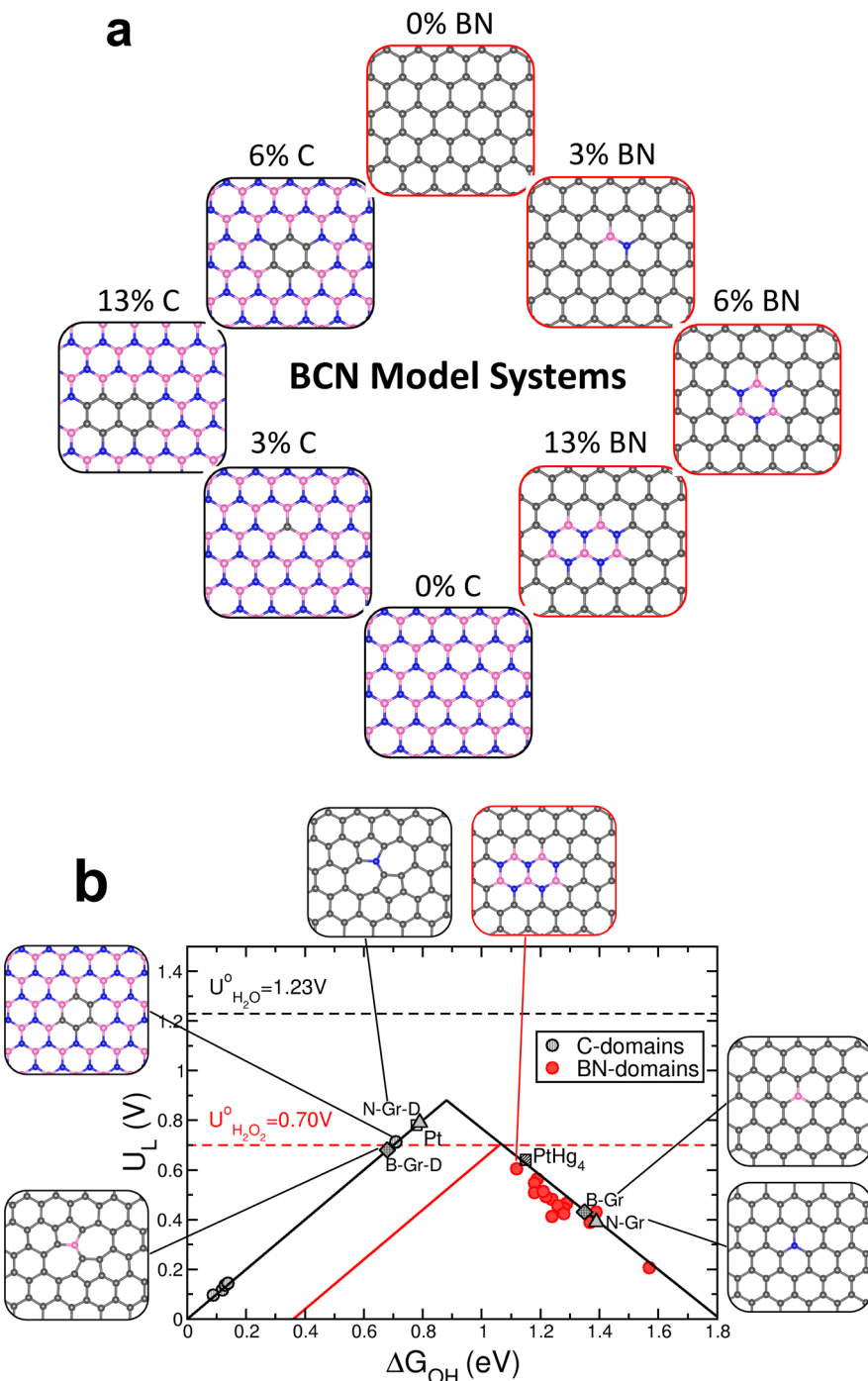


**Figure 5.** (a) Schematic of the BCN configuration models examined in this study. Color code: C, gray; N, blue; B, pink. %X composition is defined as the number of C atoms substituted in h-BN substrate over the total number of substrate atoms. Similarly, for BN domains %X composition is defined as the number of BN pairs substituted in graphene substrate over the total number of substrate atoms. (b) Theoretical activity volcano maps for 2e<sup>-</sup> (red) and 4e<sup>-</sup> (black) reduction of O<sub>2</sub> to H<sub>2</sub>O<sub>2</sub> and H<sub>2</sub>O, respectively. Both volcano plots are based on the RHE scale. The equilibrium potentials for both 2e<sup>-</sup> and 4e<sup>-</sup> ORR are shown as dashed red and black lines, respectively. Triangles or diamonds represent the activity of the N- or B-doped in the pristine (N-Gr or B-Gr) and defect (N-Gr-D or B-Gr-D) graphene, respectively. The activity of N-Gr-D is adapted from ref 44, while the activities of Pt(111) and PtHg<sub>4</sub> alloy are adapted from refs 49 and 26, respectively.

setup at 1600 rpm in O<sub>2</sub>-saturated electrolyte (Figure 4a,b). The ring electrode is made of Pt and was held at 1.2 V vs RHE to oxidize H<sub>2</sub>O<sub>2</sub> formed on the disc electrode, allowing for ORR product quantification. For the disk current, all three samples exhibited a similar onset-potential (defined as the potential at which a current density of 0.5 mA/cm<sup>2</sup> is achieved) of 0.80 V vs RHE, indicating the presence of similar

active sites within these materials. These active centers could very well be the single N-sites that are present in similar concentrations in all these samples and have previously been reported active for the 4e<sup>-</sup> ORR.<sup>44,45</sup> H<sub>2</sub>O<sub>2</sub> production is indicated by the ring current that gives a slightly lower onset potential of ca. 0.79 V vs RHE (defined as the potential at which a current density of 0.25 mA/cm<sup>2</sup> is achieved) for BN-

C1 and BN-C2. It is worth noting that a slightly higher onset potential than the thermodynamic limit of 0.7 V vs RHE is observed, and this has also been found on high surface area materials including Pt–Hg/C nanoparticles and other carbon-based materials.<sup>26,34,46</sup> This could potentially be attributed to a Nernst-related potential shift due to the low concentration of H<sub>2</sub>O<sub>2</sub> in the electrolyte, and/or a possible pH-related phenomena that we have observed for the 2e<sup>-</sup> ORR reaction previously in highly alkaline media.<sup>35</sup> On the other hand, N-C only starts to produce a similar ring current at a potential of ca. 0.67 V, much lower than that observed on B,N co-doped samples. The ORR activities of these materials normalized against electrochemical active surface area (ECSA) were also investigated and gave the same observation (Figure S4). This indicates there are distinct active centers in BN-C1 and BN-C2 that can facilitate the 2e<sup>-</sup> ORR at higher disc electrode potentials, which may arise from the unique *h*-BN domains. Therefore, the exceptionally high 2e<sup>-</sup> ORR activity for BN-C1 and BN-C2 may be assigned to the isolated *h*-BN clusters, whereby the active center for N-C is the single N-sites. For BN-C1 and BN-C2, which consists of both active-site structures, there may be competing effects for the 2e<sup>-</sup> and 4e<sup>-</sup> pathways, as shown schematically in Figure 4c. Based on our experimental characterization, BN-C1 has the largest content of *h*-BN clusters, whereas for BN-C2, a relatively lower concentration of *h*-BN is identified. This may explain why BN-C1 has the highest selectivity for H<sub>2</sub>O<sub>2</sub>, N-C has the lowest selectivity for H<sub>2</sub>O<sub>2</sub>, and BN-C2 has an intermediate selectivity. To further confirm the role of *h*-BN domains, high-temperature H<sub>2</sub> treatment at 800 °C for BN-C1 was conducted, hypothesizing H<sub>2</sub> treatment would remove some dopants and change the ORR performance. The surface area of BN-C1 after H<sub>2</sub> treatment increased from 74 m<sup>2</sup>/g to 116 m<sup>2</sup>/g, which was expected since gas treatment would remove some unstable groups and open up more pores (Figure S1a,b). As shown in Figure S2c,d, after H<sub>2</sub> treatment, most of the B and N in the form of *h*-BN motifs was removed (from 14.5 at% to 1.73 at%), whereas the concentration of single N-site encountered negligible change (from 5.29 at% to 5.74 at%). Electrochemical testing results indicate a significantly decreased H<sub>2</sub>O<sub>2</sub> selectivity after H<sub>2</sub> treatment (from 85% to 60% at 0.5 V vs RHE), which may arise from the removal of *h*-BN motifs and further suggests the important role of *h*-BN in driving the 2e<sup>-</sup> ORR for H<sub>2</sub>O<sub>2</sub> production.

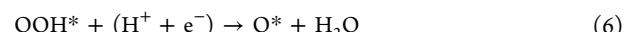
Stability is another key catalyst performance metric to consider for practical applications. Since H<sub>2</sub>O<sub>2</sub> is the major product generated, and it is a highly reactive oxidation agent, the assembled device will be subjected to harsh working conditions in comparison to conventional PEM fuel cells. Our previous work has shown that both defective carbon and N-doped carbon can exhibit stable performance for the 2e<sup>-</sup> ORR.<sup>34,35,44</sup> To evaluate the stability of the B,N co-doped carbon, a constant potential hold stability test at 0.5 V vs RHE was performed. Both the ring and disk currents were stable over 50 h (Figure 4d). We have also performed accelerated durability testing (ADT) of BN-C1 by sweeping the potential 2000 times between 0.2 and 1.1 V vs RHE at a scan rate of 200 mV/s. The catalyst experienced negligible activity loss after 2000 cycles (Figure S2). To further exam our catalyst's stability under high concentration of H<sub>2</sub>O<sub>2</sub>, the BN-C1 electrode was soaked in 0.1 M H<sub>2</sub>O<sub>2</sub> in 0.1 M KOH while rotating at 1600 rpm for 50 h. The cyclic voltammetry showed minimal changes in the activity before and after the high-

concentration H<sub>2</sub>O<sub>2</sub> soaking process (Figure S2). All these tests demonstrate our materials have promising stability.

## THEORETICAL ANALYSIS

To further understand how the *h*-BN domains in these carbon materials contribute to the observed high activity and selectivity for H<sub>2</sub>O<sub>2</sub> production, theoretical calculations were performed on a variety of possible *h*-BN/graphene interfaces (Figure 5a). The structures investigated including different size *h*-BN domains doped into a graphene lattice, and different size C domains doped into a *h*-BN lattice. In both cases, the structures are labeled as the % of total atoms attributed to the dopant domains. The complete list and details of all the studied configurations are provided in the Supporting Information (Figure S5).

Our calculations indicate that, depending on the *h*-BN/graphene structure, both the 2e<sup>-</sup> and 4e<sup>-</sup> oxygen reduction pathways are possible (eqs 1 and 4, respectively). The 2e<sup>-</sup> partial reduction pathway forming H<sub>2</sub>O<sub>2</sub> involves only OOH\* as a reaction intermediate (eqs 2 and 3), whereas the complete 4e<sup>-</sup> reduction of oxygen to water involves three intermediates (OOH\*, O\*, and OH\*) and four reduction steps (eqs 5–8).



The analysis presented herein is purely thermodynamic, which has played an essential role providing insight into the nature of active-site structures and guiding the design and optimization of various catalysts.<sup>26,28,35,44</sup> Thermodynamic predicted activity volcanoes have also been shown to be in close agreement with predicted kinetic activity volcanoes.<sup>47</sup> Therefore, there is a close connection between the kinetic and thermodynamic formulations for ORR.

Figure 5b displays the calculated limiting potential (see computational details) as a function of OH\* adsorption energy ( $\Delta G_{\text{OH}}$ ) for both the 2e<sup>-</sup> and 4e<sup>-</sup> ORR. The first step in the reduction of O<sub>2</sub> is the formation of OOH\*, which is a common intermediate in both the 2e<sup>-</sup> and 4e<sup>-</sup> pathways. As a result, the 2e<sup>-</sup> and 4e<sup>-</sup> activity volcano maps (Figure 5b) are identical on the right side (i.e., relatively weak OH\* binding energy). Previous studies suggest that materials sitting on the right leg of the 2e<sup>-</sup> volcano bind oxygen weakly ( $\Delta G_{\text{OH}} > 1.1 \text{ eV}$ ) and tend to favor H<sub>2</sub>O<sub>2</sub>, whereas materials on the left leg possess a strong thermodynamic driving force toward the H<sub>2</sub>O-forming 4e<sup>-</sup> process.<sup>26,28,35</sup> Based on our DFT results, the BCN configurations with carbon domains in a *h*-BN lattice represent strong oxygen binding energies ( $\Delta G_{\text{OH}} < 1.1 \text{ eV}$ ), which leads to further reduction of the OOH\* intermediate (eq 6) and thus the H<sub>2</sub>O-forming 4e<sup>-</sup> pathway. In all these configurations, the interface between C atoms in graphitic domains and B atoms in the *h*-BN phase is the active site, and the ORR activity varies by changing the local chemical environment of the C–B bond.

On the other hand, all of the BCN configurations with *h*-BN domains in graphene substrates bind oxygen weakly ( $\Delta G_{\text{OH}} < 1.1 \text{ eV}$ ), leading to the protonation of OOH\* to form H<sub>2</sub>O<sub>2</sub> (eq 3) as the main product. In all of these instances, a boron atom in the *h*-BN/graphene interface is the active site. The local chemical environment of the boron is the determining factor for the wide range of observed activity. It is also important to note that there is a trade-off between

activity and selectivity. Far to the right side of the volcano, activating oxygen to form  $\text{OOH}^*$  is the limiting step due to the weak interaction. Therefore, higher overpotentials and lower limiting potentials are expected for the very weak oxygen binding configurations. Among different *h*-BN concentrations, 13% *h*-BN concentration is predicted to give the best  $2\text{e}^-$  ORR performance, that comparable with PtHg<sub>4</sub>. This is in agreement with the observed high activity for BN-C1. BN-C1 is found to have about 14.5 at% of B,N co-doping concentration that is in the form of *h*-BN, close to the predicted optimal *h*-BN concentration of 13% for  $2\text{e}^-$  ORR.

As heteroatom doping is known to create a wide range of defects in carbon-based materials,<sup>48</sup> we also include the possibility of having N dopants, B dopants, and co-doped N and B (BN) in the defective carbon. Previously, we have demonstrated that N-doping in the most thermodynamically stable defects (Stone–Waals defect (55–77)) drives the  $4\text{e}^-$  reaction.<sup>44</sup> Figure 5b shows N, B, and BN dopants in defect-free graphene (labeled in Figure 5b as N-Gr, B-Gr, and BN domains, respectively) drive the  $2\text{e}^-$  process, whereas the incorporation of N and B dopants into the 55–77 defect structures (labeled in Figure 1b as N-Gr-D and B-Gr-D, respectively) leads to the  $4\text{e}^-$  reaction. Based on these theoretical results, to systematically compare the performance of B,N co-doped carbon with that of other types of carbons, B-doped carbon and defective carbon structures were also explored and were not found to be as active and selective as BN-C1 (Figure S3), which are consistent with these theoretical calculations. The performance of state-of-the-art catalyst for  $2\text{e}^-$  ORR is also summarized in Table S4. Compared with other carbon-based materials (defective carbons and N-doped carbons), BN-C1 is among the most active catalysts for  $2\text{e}^-$  ORR in base conditions. Moreover, this highly tunable BCN system opens up the possibility for the further development of catalysts with improved performance.

## CONCLUSION

In this work, we designed a facile method to prepare a series of carbon materials that consist of isolated patches of *h*-BN within the carbon framework and demonstrated these materials as promising catalysts for  $\text{H}_2\text{O}_2$  production. By tuning the initial co-monomer precursor ratios, we controlled the BET surface area and the total content of B and N dopants in the carbon structures. By applying different characterization techniques, including XPS, NEXAFS, and HRTEM, we confirm the presence of *h*-BN domains within the carbon framework of these materials, along with the coexistence of single N-doped sites, which drive the  $4\text{e}^-$  ORR in parallel and reduce the overall selectivity toward  $\text{H}_2\text{O}_2$ . We furthermore used DFT calculations and found that the interface between possible *h*-BN domains and the host graphene lattice exhibits unique catalytic behavior that preferentially drives the production of  $\text{H}_2\text{O}_2$  via the  $2\text{e}^-$  ORR, which provides understanding for the observed high activity from the as-synthesized carbon materials containing *h*-BN domains. This work involves the design and development of a new type of *h*-BN-containing carbon catalyst that is promising for the electrochemical production of  $\text{H}_2\text{O}_2$ . The insights produced for this new system also provides guidance for the design of further improved carbon catalysts.

## ASSOCIATED CONTENT

### Supporting Information

The Supporting Information is available free of charge on the ACS Publications website at DOI: [10.1021/jacs.8b02798](https://doi.org/10.1021/jacs.8b02798).

Detailed experimental procedures, characterization methods, Figures S1–S6, and Tables S1–S4 ([PDF](#))

## AUTHOR INFORMATION

### Corresponding Authors

\*[norskov@stanford.edu](mailto:norskov@stanford.edu)  
\*[jaramillo@stanford.edu](mailto:jaramillo@stanford.edu)  
\*[zbao@stanford.edu](mailto:zbao@stanford.edu)

### ORCID iD

Shucheng Chen: [0000-0002-1420-099X](https://orcid.org/0000-0002-1420-099X)

Samira Siahrostami: [0000-0002-1192-4634](https://orcid.org/0000-0002-1192-4634)

Drew Higgins: [0000-0002-0585-2670](https://orcid.org/0000-0002-0585-2670)

Xuzhou Yan: [0000-0002-6114-5743](https://orcid.org/0000-0002-6114-5743)

Thomas F. Jaramillo: [0000-0001-9900-0622](https://orcid.org/0000-0001-9900-0622)

Zhenan Bao: [0000-0002-0972-1715](https://orcid.org/0000-0002-0972-1715)

### Author Contributions

<sup>†</sup>S.C., Z.C., and S.S. contributed equally to this work.

### Notes

The authors declare no competing financial interest.

## ACKNOWLEDGMENTS

This work was supported by the U.S. Department of Energy, Office of Science, Office of Basic Energy Science, via Grant DE-SC0008685 to the SUNCAT Center of Interface Science and Catalysis. Use of Stanford Synchrotron Radiation Lightsource, SLAC National Accelerator Laboratory, is supported by the U.S. Department of Energy, Office of Science, Office of Basic Energy Science, under Contract DE-AC02-76SF00515. Part of this work was performed at the Stanford Nano Shared Facilities (SNSF), supported by the National Science Foundation under award ECCS-1542152.

## REFERENCES

- (1) Kinaci, A.; Haskins, J. B.; Sevik, C.; Çağın, T. *Phys. Rev. B: Condens. Matter Mater. Phys.* **2012**, *86*, 115410.
- (2) Dai, L.; Xue, Y.; Qu, L.; Choi, H.-J.; Baek, J.-B. *Chem. Rev.* **2015**, *115*, 4823.
- (3) Ouyang, B.; Meng, F.; Song, J. *2D Mater.* **2014**, *1*, 035007.
- (4) Duan, X.; Xu, J.; Wei, Z.; Ma, J.; Guo, S.; Wang, S.; Liu, H.; Dou, S. *Adv. Mater.* **2017**, *29*, 1701784.
- (5) Da Rocha Martins, J.; Chacham, H. *ACS Nano* **2011**, *5*, 385.
- (6) Higgins, D.; Zamani, P.; Yu, A.; Chen, Z. *Energy Environ. Sci.* **2016**, *9*, 357.
- (7) Adllan, A. A.; Dal Corso, A. *J. Phys.: Condens. Matter* **2011**, *23*, 425501.
- (8) Al-Aqtash, N.; Al-Tarawneh, K. M.; Tawalbeh, T.; Vasiliev, I. *J. Appl. Phys.* **2012**, *112*, 034304.
- (9) Ci, L.; Song, L.; Jin, C.; Jariwala, D.; Wu, D.; Li, Y.; Srivastava, A.; Wang, Z.; Storr, K.; Balicas, L.; et al. *Nat. Mater.* **2010**, *9*, 430.
- (10) Muchharla, B.; Pathak, A.; Liu, Z.; Song, L.; Jayasekera, T.; Kar, S.; Vajtai, R.; Balicas, L.; Ajayan, P. M.; Talapatra, S.; et al. *Nano Lett.* **2013**, *13*, 3476.
- (11) Silva, A.; Monticone, F.; Castaldi, G.; Galdi, V.; Alù, A.; Engheta, N. *Science* **2014**, *343*, 160.
- (12) Wu, Z. S.; Winter, A.; Chen, L.; Sun, Y.; Turchanin, A.; Feng, X.; Müllen, K. *Adv. Mater.* **2012**, *24*, 5130.
- (13) Ling, Z.; Wang, Z.; Zhang, M.; Yu, C.; Wang, G.; Dong, Y.; Liu, S.; Wang, Y.; Qiu, J. *Adv. Funct. Mater.* **2016**, *26*, 111.
- (14) Chhetri, M.; Maitra, S.; Chakraborty, H.; Waghmare, U. V.; Rao, C. *Energy Environ. Sci.* **2016**, *9*, 95.
- (15) Huang, C.; Chen, C.; Zhang, M.; Lin, L.; Ye, X.; Lin, S.; Antonietti, M.; Wang, X. *Nat. Commun.* **2015**, *6*, 7698.
- (16) Liu, Y.; Zhang, Y.; Cheng, K.; Quan, X.; Fan, X.; Su, Y.; Chen, S.; Zhao, H.; Zhang, Y.; Yu, H.; et al. *Angew. Chem., Int. Ed.* **2017**, *56*, 15607.
- (17) Zhao, Y.; Yang, L.; Chen, S.; Wang, X.; Ma, Y.; Wu, Q.; Jiang, Y.; Qian, W.; Hu, Z. *J. Am. Chem. Soc.* **2013**, *135*, 1201.

- (18) You, B.; Kang, F.; Yin, P.; Zhang, Q. *Carbon* **2016**, *103*, 9.
- (19) Wang, S.; Zhang, L.; Xia, Z.; Roy, A.; Chang, D. W.; Baek, J. B.; Dai, L. *Angew. Chem., Int. Ed.* **2012**, *51*, 4209.
- (20) Silva, R.; Voiry, D.; Chhowalla, M.; Asefa, T. *J. Am. Chem. Soc.* **2013**, *135*, 7823.
- (21) Baik, S.; Lee, J. W. *RSC Adv.* **2015**, *5*, 24661.
- (22) Wang, S.; Iyyamperumal, E.; Roy, A.; Xue, Y.; Yu, D.; Dai, L. *Angew. Chem., Int. Ed.* **2011**, *50*, 11756.
- (23) Sun, Q.; Sun, C.; Du, A.; Dou, S.; Li, Z. *Nanoscale* **2016**, *8*, 14084.
- (24) Campos-Martin, J. M.; Blanco-Brieva, G.; Fierro, J. L. *Angew. Chem., Int. Ed.* **2006**, *45*, 6962.
- (25) Viswanathan, V.; Hansen, H. A.; Rossmeisl, J.; Nørskov, J. K. *J. Phys. Chem. Lett.* **2012**, *3*, 2948.
- (26) Siahrostami, S.; Verdaguera-Casadevall, A.; Karamad, M.; Deiana, D.; Malacrida, P.; Wickman, B.; Escudero-Escribano, M.; Paoli, E. A.; Frydendal, R.; Hansen, T. W.; et al. *Nat. Mater.* **2013**, *12*, 1137.
- (27) Marković, N.; Adić, R.; Vešović, V. *J. Electroanal. Chem. Interfacial Electrochem.* **1984**, *165*, 121.
- (28) Verdaguera-Casadevall, A.; Deiana, D.; Karamad, M.; Siahrostami, S.; Malacrida, P.; Hansen, T. W.; Rossmeisl, J.; Chorkendorff, I.; Stephens, I. E. *Nano Lett.* **2014**, *14*, 1603.
- (29) Jirkovský, J. S.; Panas, I.; Ahlberg, E.; Halasa, M.; Romani, S.; Schiffrin, D. J. *J. Am. Chem. Soc.* **2011**, *133*, 19432.
- (30) Park, J.; Nabae, Y.; Hayakawa, T.; Kakimoto, M.-a *ACS Catal.* **2014**, *4*, 3749.
- (31) Liu, Y.; Quan, X.; Fan, X.; Wang, H.; Chen, S. *Angew. Chem., Int. Ed.* **2015**, *54*, 6837.
- (32) Lee, Y.-H.; Li, F.; Chang, K.-H.; Hu, C.-C.; Ohsaka, T. *Appl. Catal., B* **2012**, *126*, 208.
- (33) Fellinger, T.-P.; Hasché, F. d. r.; Strasser, P.; Antonietti, M. *J. Am. Chem. Soc.* **2012**, *134*, 4072.
- (34) Chen, Z.; Chen, S.; Siahrostami, S.; Chakthranont, P.; Hahn, C.; Nordlund, D.; Dimosthenis, S.; Nørskov, J. K.; Bao, Z.; Jaramillo, T. F. *Reaction Chemistry & Engineering* **2017**, *2*, 239.
- (35) Chen, S.; Chen, Z.; Siahrostami, S.; Kim, T. R.; Nordlund, D.; Sokaras, D.; Nowak, S. H.; To, J. W.; Higgins, D. C.; Sinclair, R.; et al. *ACS Sustainable Chem. Eng.* **2018**, *6*, 311.
- (36) To, J. W.; Chen, Z.; Yao, H.; He, J.; Kim, K.; Chou, H.-H.; Pan, L.; Wilcox, J.; Cui, Y.; Bao, Z. *ACS Cent. Sci.* **2015**, *1*, 68.
- (37) Pan, L.; Yu, G.; Zhai, D.; Lee, H. R.; Zhao, W.; Liu, N.; Wang, H.; Tee, B. C.-K.; Shi, Y.; Cui, Y.; et al. *Proc. Natl. Acad. Sci. U. S. A.* **2012**, *109*, 9287.
- (38) Deore, B. A.; Yu, I.; Aguiar, P. M.; Recksiedler, C.; Kroeker, S.; Freund, M. S. *Chem. Mater.* **2005**, *17*, 3803.
- (39) Schiros, T.; Nordlund, D.; Palova, L.; Zhao, L.; Levendorf, M.; Jaye, C.; Reichman, D.; Park, J.; Hybertsen, M.; Pasupathy, A. *ACS Nano* **2016**, *10*, 6574.
- (40) Brühwiler, P.; Maxwell, A.; Puglia, C.; Nilsson, A.; Andersson, S.; Mårtensson, N. *Phys. Rev. Lett.* **1995**, *74*, 614.
- (41) Hemraj-Benny, T.; Banerjee, S.; Sambasivan, S.; Fischer, D. A.; Han, W.; Misewich, J. A.; Wong, S. S. *Phys. Chem. Chem. Phys.* **2005**, *7*, 1103.
- (42) Shimoyama, I.; Wu, G.; Sekiguchi, T.; Baba, Y. *Phys. Rev. B: Condens. Matter Mater. Phys.* **2000**, *62*, R6053.
- (43) Schiros, T.; Nordlund, D.; Pálová, L.; Prezzi, D.; Zhao, L.; Kim, K. S.; Wurstbauer, U.; Gutiérrez, C.; Delongchamp, D.; Jaye, C.; et al. *Nano Lett.* **2012**, *12*, 4025.
- (44) To, J. W.; Ng, J. W. D.; Siahrostami, S.; Koh, A. L.; Lee, Y.; Chen, Z.; Fong, K. D.; Chen, S.; He, J.; Bae, W.-G.; et al. *Nano Res.* **2017**, *10*, 1163.
- (45) Guo, D.; Shibuya, R.; Akiba, C.; Saji, S.; Kondo, T.; Nakamura, J. *Science* **2016**, *351*, 361.
- (46) Brocato, S.; Serov, A.; Atanassov, P. *Electrochim. Acta* **2013**, *87*, 361.
- (47) Hansen, H. A.; Viswanathan, V.; Nørskov, J. K. *J. Phys. Chem. C* **2014**, *118*, 6706.
- (48) Hou, Z.; Wang, X.; Ikeda, T.; Terakura, K.; Oshima, M.; Kakimoto, M.-a.; Miyata, S. *Phys. Rev. B: Condens. Matter Mater. Phys.* **2012**, *85*, 165439.
- (49) Nørskov, J. K.; Rossmeisl, J.; Logadottir, A.; Lindqvist, L.; Kitchin, J. R.; Bligaard, T.; Jonsson, H. *J. Phys. Chem. B* **2004**, *108*, 17886.